

All optical ultrafast probe of a topological phase transition

R. E. F. Silva^{1,2,†}, Á. Jiménez-Galán^{1,††}, B. Amorim³, O. Smirnova^{1,4}, & M. Ivanov^{1,5,6}

¹*Max-Born-Institute, Max-Born Straße 2A, D-12489 Berlin, Germany.*

²*Department of Theoretical Condensed Matter Physics, Universidad Autónoma de Madrid, E-28049 Madrid, Spain*

³*CeFEMA, Instituto Superior Técnico, Universidade de Lisboa, Av. Rovisco Pais, 1049-001 Lisboa, Portugal*

⁴*Technische Universität Berlin, Ernst-Ruska-Gebäude, Hardenbergstraße 36A, 10623 Berlin, Germany.*

⁵*Department of Physics, Humboldt University, Newtonstraße 15, D-12489 Berlin, Germany.*

⁶*Blackett Laboratory, Imperial College London, South Kensington Campus, SW7 2AZ London, United Kingdom.*

† silva@mbi-berlin.de †† jimenez@mbi-berlin.de

High harmonic spectroscopy provides fundamental insight into the electronic structure and dynamics of matter. Initially developed as a probe of atomic and molecular targets, it has now begun to shed light onto fundamental properties of condensed matter systems, opening the way for ultrafast optical probing of solid state materials. One of the most fascinating recent developments in condensed matter is the possibility that certain systems can sustain robust chiral edge states, which are protected by topologically invariant quantities of the

bulk system. Here we show that high harmonic spectroscopy offers an all-optical probe for the characterization of topologically distinct phases of matter. We use the nonlinear optical response to map out the phase diagram across a topological phase transition in the 2D Chern insulator famously proposed by Haldane. Our work opens a new route for the detection of topological invariants in matter on an ultrafast time-scale.

1 Introduction

High harmonic generation (HHG) provides fundamental insights into the electronic structure and dynamics of different systems ¹. Initially developed to study atomic and molecular gases ^{2,3}, HHG has now been extended into condensed matter systems ⁴. While high harmonic generation provides robust table-top source of coherent, ultrafast pulses in ultraviolet, extreme ultraviolet, and soft X-ray range (see, for example, ^{1,5}) with tunable duration, carrier, spin and optical angular momentum properties ⁶⁻¹⁰, it also stands out as a spectroscopic tool for ultrafast dynamics in molecules with sub-100 attosecond temporal resolution ¹¹⁻¹⁶. High harmonic spectroscopy has now made important steps towards ultrafast characterization of fundamental processes in condensed matter systems. Examples include the observation of dynamical Bloch oscillations ^{17,18}, band structure tomography ^{19,20}, and resolving electron-hole dynamics ^{17,21,22}, including dynamics in strongly correlated systems and phase transitions in the Mott insulator ²³, the Peierls phase transition ²², or the imprint of the Berry phase on high harmonic spectrum ^{24,25}.

Historically, high harmonic spectroscopy in atoms and molecules first highlighted the role of the ionization potential in the strong field optical response ^{2,3}. Similarly, HHG spectroscopy

in solids has first established the key role of the material band structure for its ultrafast optical response ²⁶. Recently, however, nonlinear response in atoms and molecules was found to also depend dramatically on the angular momentum, ring currents, and the chirality of the initial and final states ^{27–32}. In the condensed phase, one of the most fascinating features of novel 2D systems is the presence of chiral-edge states in topological insulators. Here we show how high harmonic spectroscopy tracks the appearance of such chiral-edge states and how it can, therefore, serve as an all-optical probe of a topological phase transition.

In topological materials, the bulk is an insulator but the surface supports gapless chiral-edge states, which carry charge along a single direction. This makes these materials appealing for many applications, ranging from the development of dissipationless devices to the creation of topologically robust superconductors ^{33,34}. Importantly, the chiral-edge states are protected by topological invariants of the bulk system. One such topological invariant is the Chern number, which is given by the integral of the Berry curvature along the 2D-Brillouin zone of the filled bands. The Chern number is an integer and it is proportional to the Hall conductivity, leading to the quantization of the latter. States of matter characterized by a non-zero Chern number, and thus supporting topologically protected chiral edge-states, are known as Chern insulators.

The first and clearest example of a Chern insulator was proposed by Haldane in his seminal paper ³⁵, in which he proposed a model to realize the quantum Hall effect on a graphene-like structure without an external magnetic field (quantum anomalous Hall effect). The model contained two key ingredients. First, inversion symmetry was broken by placing two different atoms, A and B, at

neighbouring sites with on-site energy $+M$ and $-M$, respectively, leading to a gap opening at the Dirac cones \mathbf{K} and \mathbf{K}' (Fig. 1c). Second, time-reversal symmetry was broken by adding complex second-nearest-neighbour hoppings with the positive phase of the hoppings following a specific chiral direction (Fig. 1a). This hopping acts as a local magnetic field, which is zero on average and has the symmetry of the lattice. This system is in a trivial insulating state with zero Chern number if $|M/(3\sqrt{3})| > t_2 \sin \phi$, but it becomes topological when $|M/(3\sqrt{3})| < t_2 \sin \phi$, giving rise to a Chern number of ± 1 , and therefore to a non-zero Hall conductivity and the appearance of gapless edge states (see Fig. 1b). This model, which has now become the paradigm of topological insulators, is also the starting point for the study of several phenomena linked to topological properties of materials, for example, the quantum spin Hall effect ³⁶ or the valley Hall effect ³⁷. First perceived as being "unlikely to be directly physically realizable" ³⁵, the Haldane model has now been demonstrated experimentally in an optical lattice ³⁸.

Here we provide an ultrafast all-optical characterization of the topological phase transition that occurs in 2-D Chern insulators. We study the high harmonic response in the Haldane model in its trivial and topological phases. We show that the helicity of high harmonics changes during the phase transition, and that the phase diagram can be extracted by measuring the helicity of the odd high harmonics relative to the helicity of the first harmonic, providing a simple all-optical way to map the Chern number. The characterization of topological invariants in solids using high harmonic generation is a first step towards ultrafast petahertz electronics in topological materials ⁴⁰.

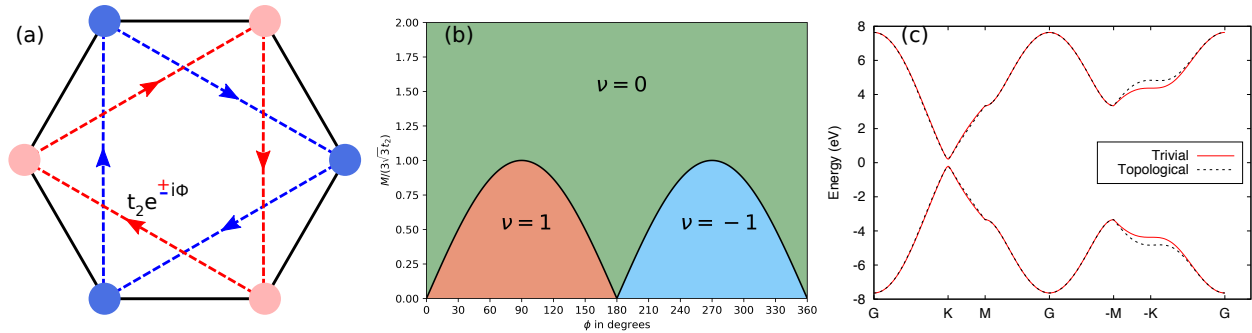


Figure 1: **Haldane model**. (a) Honeycomb structure in real space. Two different atoms (blue- and red-colored) break inversion symmetry. Dashed lines indicate second-neighbour complex hoppings $t_2 e^{\pm i\phi}$. The red dashed lines show the positive phase hopping while the blue dashed lines show the negative phase hopping. (b) Phase diagram of Haldane model. The phase transition occurs at $\tau \equiv M/(3\sqrt{3}t_2 \sin \phi) = 1$, where $|M|$ is the on-site energy of the atoms. The system behaves as a trivial insulator for $\tau > 1$, as a topological insulator with Chern number $\nu = +1$ when $\tau < 1$ and $\phi < 180^\circ$, and as a topological insulator with $\nu = -1$ when $\tau < 1$ and $\phi > 180^\circ$. (c) Bulk band structure in a trivial ($\tau = 1.1$, red solid) and topological ($\tau = 0.9$, black dashed) insulator.

2 Results

We consider the interaction of a moderately strong ($E_0 = 4 \times 10^9$ V/m), mid-IR ($\lambda = 3 \mu\text{m}$) pulse (pulse duration 30fs), linearly polarized in the \hat{e}_y direction, with the honeycomb structure depicted in Fig. 1a. The light frequency is well below the bandgap, so that the interaction is in the low-frequency, strong-field regime. To calculate the response, we solve the semiconductor Bloch equations for the Haldane tight-binding model. We start with a filled valence band and an empty conduction band and we propagate the density matrix in the Wannier gauge in the presence of the infrared field on a grid with 300 points in the k_x direction and 300 points in the k_y direction, using a uniform time step of 0.1 atomic units (a.u.). Our aim is to show that the high harmonic response provides a unique footprint of the topological phase transition, that is, of the phase diagram in Fig. 1b.

The tight-binding Haldane Hamiltonian used $t_1 = 0.089$ a.u., $a = 2.73$ Å and $M = 0.084$ a.u. for the nearest-neighbour hoppings, distance between neighbouring atoms and on-site energy of each atom, respectively, to mimic a single layer of hexagonal boron nitride using the well-known two band model⁴¹. The amplitude and phase of the complex second-neighbour-hoppings were varied from $0.1 < M/(3\sqrt{3}t_2) < 2$ and from $0 < \phi < 2\pi$, thus covering the full phase diagram in Fig. 1b, which includes both trivial and topological phases. Fig. 1c shows the structure of the valence and conduction bands in the Haldane model for the trivial [$M/(3\sqrt{3}t_2) = 1.1, \sin \phi = 1$] and topological [$M/(3\sqrt{3}t_2) = 0.9, \sin \phi = 1$] states of matter, which essentially coincide. This shows that one cannot characterize the phase diagram of the system from an observable that only

depends on the bulk band structure.

This conclusion is further illustrated in panels (a) and (b) of Fig. 2, which show the electron density in the conduction band after the interaction with the field, for the trivial and topological phases shown in Fig. 1c. In the low-frequency regime, the excitation to the conduction bands occurs dominantly at the \mathbf{K} -point, where the band gap is minimum for the chosen parameters. As with the band structure, both trivial and topological phases show the same behaviour: the electron densities are localized at the same crystal momenta and with the same magnitude, providing no indication of the topological phase transition.

We now turn to the non-linear optical response, shown in Fig. 2 panels (c) and (d). For the same trivial and topological insulators as before, the helicity of the harmonic emission shows clear difference between the two phases. In panels (c,d) we have separated the high harmonic emission into the two helical components: I_{\odot} and I_{\ominus} , where $I_{\odot} \equiv |\mathbf{D}(\omega) \cdot \hat{e}_+|^2$ corresponds to light rotating clockwise, and $I_{\ominus} \equiv |\mathbf{D}(\omega) \cdot \hat{e}_-|^2$ to light rotating counter-clockwise, with $\hat{e}_{\pm} = -(\hat{e}_x \mp i \hat{e}_y)/\sqrt{2}$ being the unit vectors in the circular basis and $\mathbf{D}(\omega)$ the frequency dipole, which is defined as the Fourier transform of the current density (see Methods). While the fundamental harmonic has the same helicity in both trivial and topological phases, the odd high order harmonics change their helicity upon the phase transition. In the trivial phase, they co-rotate with the fundamental, while they counter-rotate in the topological phase.

Since this effect is evident from the third harmonic, to uncover its origin we consider the semi-classical response. The insets in Fig. 2c,d show that the current obtained using a semiclassical

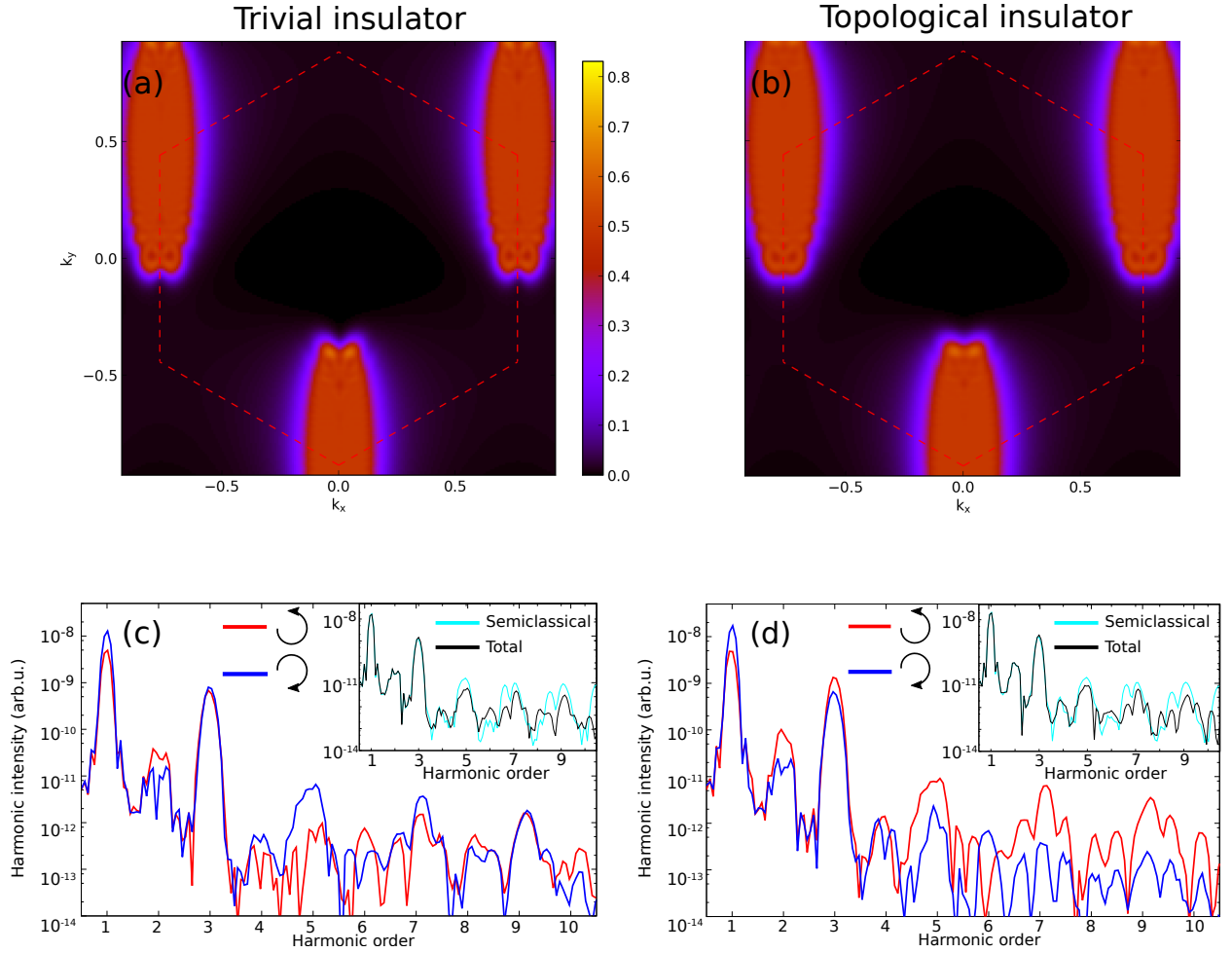


Figure 2: **Optical linear and non-linear response from trivial and topological insulators.** Top panels: electron density for a trivial (a) and a topological insulator (b) show no clear sign of the phase transition. Bottom panels: HHG emission separated into the two circular components, I_{\odot} (red) and I_{\ominus} (blue). Odd harmonics rotate in the same direction as the fundamental in the trivial insulator (c), but in opposite direction in the topological phase (d). The insets in (c) and (d) compare the semiclassical response (cyan) with the full quantum response (black).

approach (see Methods) provides a good description for moderately energetic high harmonics. The optical response of bulk solids to strong laser fields is proportional to the Fourier transform of the current density,

$$\mathbf{D}(\omega) \propto \int \mathbf{J}(t) e^{i\omega t} dt. \quad (1)$$

In the semi-classical analysis it is common to separate the current density into two terms ⁴² (see Methods for details):

$$\mathbf{J}(t) = \mathbf{j}_{\text{intra}}(t) + \mathbf{j}_{\text{anom}}(t). \quad (2)$$

The first term is the intraband current, which depends essentially on the band structure. Since the latter is nearly identical just before and just after the phase transition, the intraband current cannot be responsible for the different chiral response we observe. The second term is the anomalous current, which depends on the Berry curvature. Intuitively, the Berry curvature at the \mathbf{K} and \mathbf{K}' points acts like a local magnetic field pointing in the direction perpendicular to the 2D plane (\hat{e}_z) and deflecting the electrons to $\pm\hat{e}_x$ depending on its sign (and the sign of the oscillating electric field $\mathbf{E}(t)$). This deflection generates a rotating current with the direction of rotation, and hence the helicity of the emitted light, given by the sign of the Berry curvature. The latter changes upon the topological phase transition and it is this sign change that the high harmonics probe.

Fig. 3a illustrates the effect. For $0 < \phi < \pi$, the minimum band gap is located at \mathbf{K} . For a trivial insulator, the points \mathbf{K} and \mathbf{K}' have Berry curvatures with opposite signs. This means that for a full valence band, electrons rotating at \mathbf{K} will cancel with those rotating at \mathbf{K}' , giving no net anomalous current for this band. In other words, the Chern number is zero. Thus, both the linear and non-linear optical responses in the trivial phase are generated by the electron-hole pair current

created by the low-frequency laser field near the \mathbf{K} point, where the band gap is minimum. The anomalous current rotates following the sign of the Berry curvature at \mathbf{K} , as depicted in Fig. 3a.

When the system undergoes the phase transition and becomes topological, the gap closes at \mathbf{K} , and the Berry curvature at \mathbf{K} changes sign. Now, the Berry curvatures at points \mathbf{K} and \mathbf{K}' have the same sign, generating non-zero net current in the valence band, reflected in a Chern number equal to +1 or -1. In this case, the linear response is dominated by the sign of the Hall conductivity. The latter is the same as the sign of the Berry curvature at the excitation point \mathbf{K} in the trivial phase ("+" in Fig. 3a), but opposite in the topological phase. High harmonics, on the other hand, result from the excitation to the conduction band and reflect the current generated by the electron-hole pairs at \mathbf{K} , where the sign of the Berry curvature is opposite to both the sign of the Hall conductivity in the topological phase and the Berry curvature at \mathbf{K} in the trivial phase (see Fig. 3a).

This clear physical picture is supported by the simple analytical model of the semi-classical current. The intraband current is directed mainly along the direction of the electric field (\hat{e}_y), while the anomalous current is directed along \hat{e}_x . Hence, to a good approximation we may write the optical response of the N -th harmonic as

$$\mathbf{D}(N\omega) \propto [\tilde{\mathbf{j}}_{\text{anom}}(N\omega) \cdot \hat{e}_x] \hat{e}_x + [\tilde{\mathbf{j}}_{\text{intra}}(N\omega) \cdot \hat{e}_y] \hat{e}_y, \quad (3)$$

where the tilde indicates the Fourier transform of the current. As stated earlier, the intraband component has the same behaviour for the topological and trivial phases owing to the similarity of the band structure; in particular, the current along \hat{e}_y remains approximately the same across the

phase transition. Thus, the flip in the helicity of high harmonics during the phase transition has to come from the sign change in the anomalous current. Let us assume that the electron density in the conduction band is a small fraction Δ of the total electron density. Upon the excitation to the conduction band in a low-frequency field, it will be localized near the point $\mathbf{k} = \mathbf{K}$ where the band gap is minimum. It is then easy to show (see Methods) that the Fourier transform of the anomalous current in the long-pulse limit is

$$\tilde{\mathbf{j}}_{\text{anom}}(N\omega) \cdot \hat{e}_x = -2\pi |e|^2 E_0 \left\{ \frac{2\pi\mathcal{C}}{V_{\text{BZ}}} \delta_{1N} - 2\Delta \sum_{\mathbf{R} \in \text{BL}} e^{i\mathbf{K} \cdot \mathbf{R}} \Omega(\mathbf{R}) [J_{N-1}(\mathbf{A}_0 \cdot \mathbf{R}) + J_{N+1}(\mathbf{A}_0 \cdot \mathbf{R})] \right\}. \quad (4)$$

In the above, $\mathcal{C} = \frac{1}{2\pi} \int_{\text{BZ}} d^2\mathbf{k} \Omega(\mathbf{k})$ is the Chern number, V_{BZ} is the volume of the Brillouin zone, δ_{1N} is the Kronecker delta, which is zero for $N \neq 1$ harmonics, $\Omega(\mathbf{R}) = \sum_{\mathbf{k}} e^{i\mathbf{k} \cdot \mathbf{R}} \Omega(\mathbf{k})$ is the Berry curvature of the valence band in position space, J_n is the n -th Bessel function of the first kind, and \mathbf{A}_0 is the vector potential of the laser electric field.

Equation 4 encodes the physics behind our results. While high order harmonics ($N > 1$) are insensitive to the topology of the system, that is, to the Chern number, the fundamental field ($N = 1$) is not. The sign of the second term in Eq. 4 is negative of the Berry curvature in the valence band (see Methods). In the trivial insulating state, the Chern number and thus the first term are equal to zero. Hence, the sign of the anomalous current for all harmonics (including the fundamental) is dictated by the sign of the second term of Eq. 4, that is, by the negative of the Berry curvature at the excitation point \mathbf{K} (see Fig. 3a). In the topologically non-trivial state, high order harmonics will also follow the negative Berry curvature, which has now flipped the sign,

triggering the change in the harmonic's helicity. However, the Chern number is now non-zero, and for small Δ the first term dominates the anomalous current contribution to the linear response. In the topologically non-trivial phase, the sign of the Chern number is always the same as that of the valence band Berry curvature. Eq. 4 thus explains why only higher order harmonics, and not the fundamental, change the sign of their response between the trivial and the topological cases.

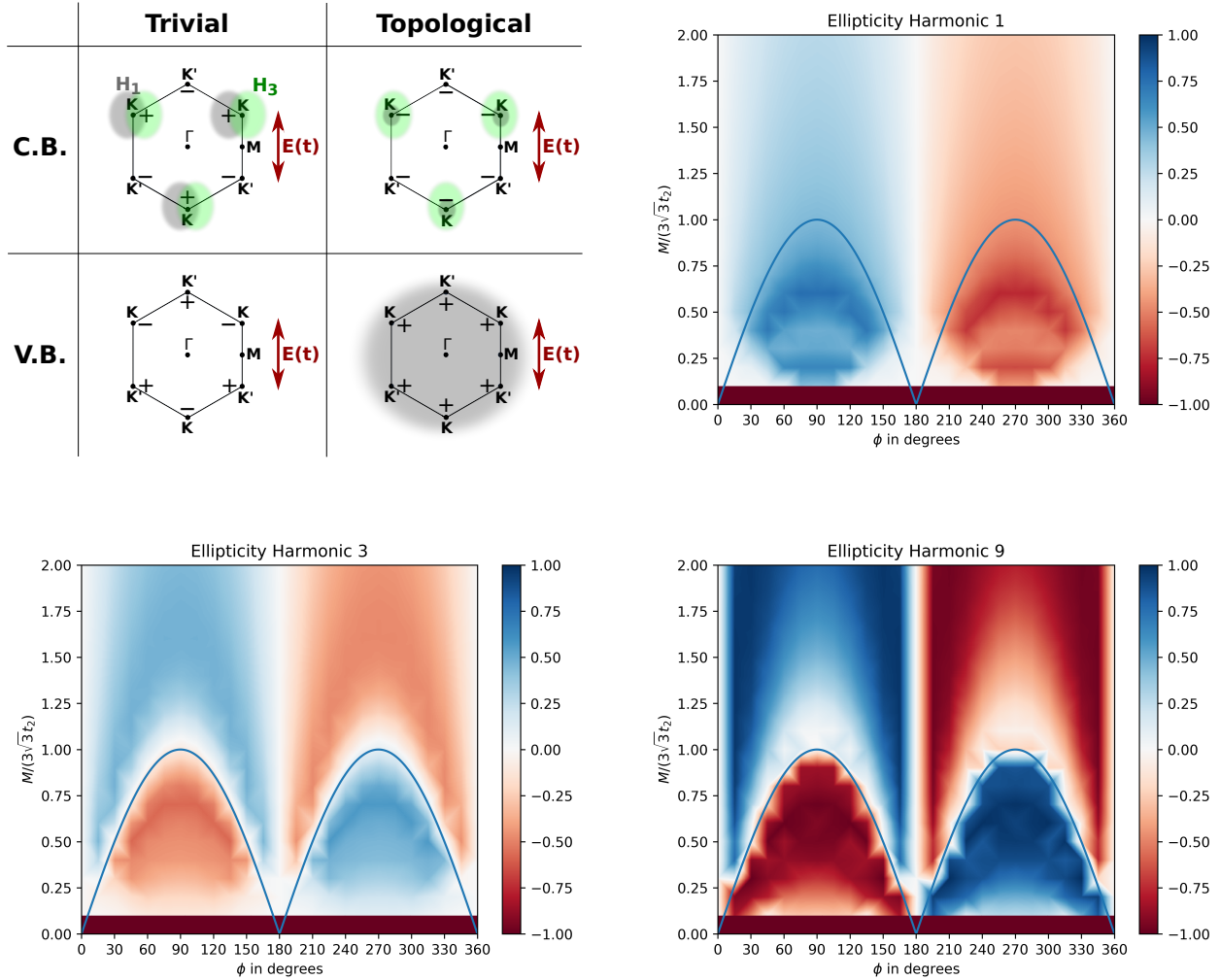


Figure 3: **Ellipticity of harmonics in topological insulators.** Top left: Scheme of the regions in the Brillouin zone probed by the first harmonic (grey shadow) and high harmonics (green shadow), see text for details. Ellipticity as defined by Eq. 5 of the first (top right), third (bottom left) and ninth (bottom right) harmonics as a function of the amplitude t_2 and phase ϕ of the second nearest neighbour hopping. The blue line indicates the topological phase transition.

This behaviour is common to all relevant values of $t_2 e^{i\phi}$. Indeed, in Fig. 3b-d we plot the

helicity of three harmonics (fundamental, third, and ninth) as a function of t_2 and ϕ . The helicity is computed as

$$e = \frac{I_{\mathcal{C}} - I_{\mathcal{O}}}{I_{\mathcal{C}} + I_{\mathcal{O}}}, \quad (5)$$

where we take the energy-integrated intensity I of the harmonic, as it would be done in an experiment, over an interval of half the frequency of the driving laser to the left and to the right of the nominal value of the harmonic. In Fig. 3b-d we show the phase transition between the trivial and the topological insulators with the solid blue line. We see that the first harmonic does not change the helicity when passing through the topological phase transition. In contrast, the non-linear response experiences a sudden change in the sign of the helicity when the material becomes topological. The observable

$$\mathcal{E} = \frac{\text{sgn}(e_{H1}) - \text{sgn}(e_{H3})}{2}, \quad (6)$$

unambiguously shows if the system is trivial or topological in an all-optical way. This quantity exactly coincides with the Chern number in Haldane's model. Figure 4 shows this observable, for all relevant values of t_2 and ϕ , that accurately reproduces the phase diagram of 2-D topological insulators.

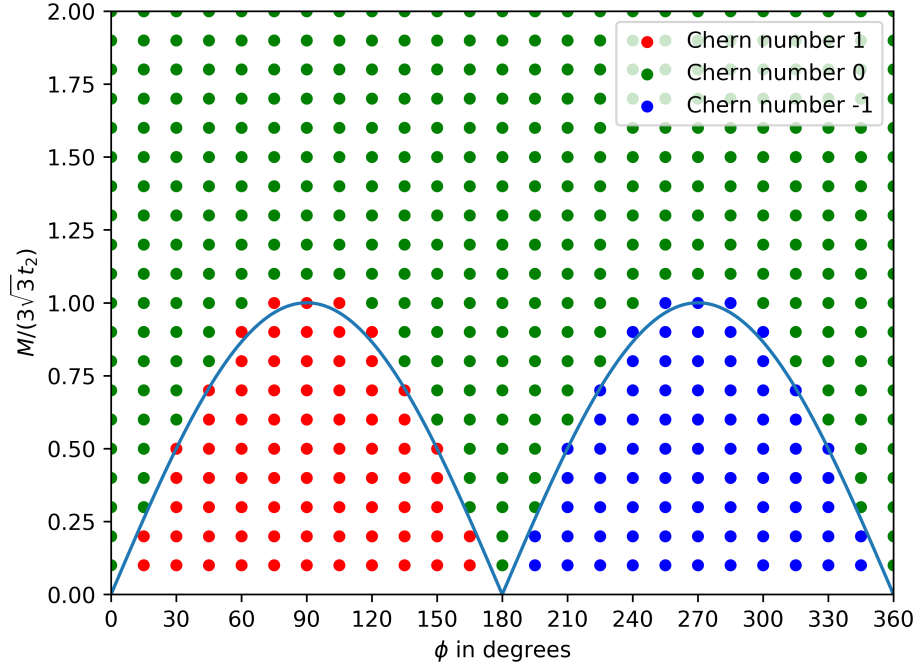


Figure 4: **Optical retrieval of Chern number.** Phase diagram of the Haldane model obtained by using Eq. 6. Each point is a calculation. Green points indicate $\mathcal{E} = 0$, red points $\mathcal{E} = 1$ and blue points $\mathcal{E} = -1$, which coincide with the value of the Chern number. The blue solid line represents the topological phase transition.

In conclusion, we have demonstrated the capability of HHG spectroscopy to probe and characterize the Chern number in the Haldane model. Our all-optical method permits to retrieve the complete phase diagram of Chern insulators with high accuracy. With the aid of a simple model we have seen that the relation of the ellipticities between the high order harmonics, that probe the sign of the Berry curvature in the conduction band, and the first harmonic, that probes the topology of the system, allows us to map the phase diagram of the prototypical 2-D Chern insulator. We have tested the robustness of this approach for different laser intensities, frequencies and durations,

obtaining equal results. Our work provides the first steps towards the use of high harmonic spectroscopy to characterize topological invariants in the condensed phase, opening the way towards ultrafast monitor and control of topological systems with strong laser fields.

Methods

Here we derive the semiclassical expression given in Eq. 4 given of the main body. In length gauge and in dipole approximation, the Hamiltonian of our system can be written as

$$\hat{H}(t) = \frac{\hat{\mathbf{p}}^2}{2m} + U + |e|\mathbf{E}(t) \cdot \hat{\mathbf{r}}, \quad (7)$$

where U has the periodicity of the crystal and the the time-independent Hamiltonian $\hat{H}_0 = \frac{\hat{\mathbf{p}}^2}{2m} + U$ satisfies

$$\hat{H}_0|\psi_{n\mathbf{k}}\rangle = \varepsilon_n(\mathbf{k})|\psi_{n\mathbf{k}}\rangle. \quad (8)$$

The indices \mathbf{k} and n indicate the crystal momentum and band number, respectively. The eigenfunctions $\psi_{n\mathbf{k}}$ are the Bloch wavefunctions, which are written as

$$\psi_{n\mathbf{k}}(\mathbf{r}) = e^{i\mathbf{k}\cdot\mathbf{r}}u_{n\mathbf{k}}(\mathbf{r}), \quad (9)$$

where $u_{n\mathbf{k}}(\mathbf{r})$ is a function with the periodicity of the crystal.

The laser field $\mathbf{E}(t)$ is linearly polarized in the \hat{e}_y direction and, for simplicity, it is assumed to be monochromatic,

$$\mathbf{E}(t) = E_0 \left(e^{i\omega x t} + e^{-i\omega x t} \right) \hat{e}_y. \quad (10)$$

The high harmonic spectrum is proportional to the Fourier transform of the average current

density, the frequency dipole:

$$\mathbf{D}(\omega) \propto \int e^{i\omega t} \mathbf{J}(t) dt, \quad (11)$$

where the average current density has the form

$$\mathbf{J}(t) = -|e| \sum_{\mathbf{k} \in \text{BZ}} \text{Tr}[\mathbf{v}_{\mathbf{k}} \rho(\mathbf{k}, t)], \quad (12)$$

and the sum runs over all crystal momentum belonging to the first Brillouin zone. The velocity can be written as

$$\mathbf{v}_{\mathbf{k}} = -i [\hat{\mathbf{r}}, \hat{H}(\mathbf{k}, t)], \quad (13)$$

while the density matrix $\rho(\mathbf{k}, t)$ obeys the equation of motion

$$\frac{\partial}{\partial t} \hat{\rho}(t) = -i [\hat{H}(t), \hat{\rho}(t)], \quad \hat{\rho}(0) = \sum_n \sum_{\mathbf{k} \in \text{BZ}} p_{n,\mathbf{k}} |\psi_{n\mathbf{k}}\rangle \langle \psi_{n\mathbf{k}}|, \quad (14)$$

where $p_{n\mathbf{k}}$ is the occupation number of the state $\psi_{n\mathbf{k}}$.

In (12), both the velocity and density matrix are matrices of $N \times N$ dimension, where N is the number of bands. Adopting the semi-classical approximation, we write the velocity matrix as diagonal, that is, we assume electrons in different bands are non-interacting. The equations of motion for an electron restricted to move in band n under the influence of an electromagnetic field $\mathbf{E}(t)$ are

$$\begin{aligned} \dot{\mathbf{k}} &= -|e| \mathbf{E}(t), \\ \dot{\mathbf{r}} &= \nabla_{\mathbf{k}} \varepsilon_n(\mathbf{k}) - \dot{\mathbf{k}} \times \Omega_{nn}(\mathbf{k}), \end{aligned} \quad (15)$$

where $\Omega_{nn}(\mathbf{k}) = \nabla \times A_{nn}(\mathbf{k})$ is the Berry curvature of the band and $A_{nn}(\mathbf{k}) = i \langle u_{n\mathbf{k}} | \nabla_{\mathbf{k}} u_{n\mathbf{k}} \rangle$ is the Berry connection. In our case, the Berry connection has components in \hat{e}_x and \hat{e}_y , and hence the

Berry curvature is oriented along \hat{e}_z . Introducing (15) in (12), we obtain that the average current density in the semiclassical approximation can be written as

$$\mathbf{J}(t) = -|e| \sum_n \sum_{\mathbf{k} \in \mathbf{BZ}} [\nabla_{\mathbf{k}} \varepsilon_n(\mathbf{k}) + |e| \mathbf{E}(t) \times \Omega_{nn}(\mathbf{k})] \rho_{nn}(\mathbf{k}, t). \quad (16)$$

Above, the first term is the intraband term and the second term is the anomalous current.

Let us consider now only two bands: the valence band (-) and the conduction band (+). We assume that the laser induces a small fraction Δ_p of electron population per site to be transferred from the valence to the conduction band at the point $\mathbf{k} = \mathbf{K}$, where the laser is oriented, and that the electron momentum follows adiabatically the vector potential, such that

$$\hat{\rho}_{nn}(\mathbf{k}, t) = \begin{cases} N_{\mathbf{k}} \Delta_p \delta_{\mathbf{k}, (\mathbf{K} - \mathbf{A}(t))} & n = (+) \\ 1 - N_{\mathbf{k}} \Delta_p \delta_{\mathbf{k}, (\mathbf{K} - \mathbf{A}(t))} & n = (-), \end{cases} \quad (17)$$

where $N_{\mathbf{k}}$ is the number of sites or, equivalently, the number of k-points of the system. The normalization is taken so that $\sum_n \sum_{\mathbf{k} \in \mathbf{BZ}} \rho_{nn}(\mathbf{k}, t) = N_{\mathbf{k}}$. In this case, the average current normalized to the number of sites, $\bar{\mathbf{J}}(t) \equiv \mathbf{J}(t)/N_{\mathbf{k}}$, is

$$\begin{aligned} \bar{\mathbf{J}}(t) = -|e| & \left\{ \Delta_p \left[\nabla_{\mathbf{k}} \varepsilon_+(\mathbf{k})|_{\mathbf{K} - \mathbf{A}(t)} + |e| \mathbf{E}(t) \times \Omega_+(\mathbf{K} - \mathbf{A}(t)) \right] \right. \\ & - \Delta_p \left[\nabla_{\mathbf{k}} \varepsilon_-(\mathbf{k})|_{\mathbf{K} - \mathbf{A}(t)} + |e| \mathbf{E}(t) \times \Omega_-(\mathbf{K} - \mathbf{A}(t)) \right] \\ & \left. + \frac{1}{N_{\mathbf{k}}} \sum_{\mathbf{k} \in \mathbf{BZ}} \left[\nabla_{\mathbf{k}} \varepsilon_-(\mathbf{k}) + |e| \mathbf{E}(t) \times \Omega_-(\mathbf{k}) \right] \right\} \end{aligned} \quad (18)$$

It can be proven that ⁴³

$$\sum_{\mathbf{k} \in \mathbf{BZ}} \nabla_{\mathbf{k}} \varepsilon_-(\mathbf{k}) = 0, \quad (19)$$

since $\epsilon_-(\mathbf{k})$ is a periodic function. Also, since $\sum_n \Omega_n(\mathbf{k}) = 0$, we have $\Omega_-(\mathbf{k}) = -\Omega_+(\mathbf{k}) \equiv \Omega(\mathbf{k})$.

Finally, we can identify the Chern number \mathcal{C} ,

$$\sum_{\mathbf{k} \in \mathbf{BZ}} \Omega_-(\mathbf{k}) = \frac{N_{\mathbf{k}}}{V_{BZ}} \int_{\mathbf{k} \in BZ} \Omega_-(\mathbf{k}) d\mathbf{k} = \frac{2\pi \mathcal{C}_-}{V_{BZ}}, \quad (20)$$

where we have used $1/N_{\mathbf{k}} \sum_{\mathbf{k} \in BZ} = 1/V_{BZ} \int_{\mathbf{k}} d\mathbf{k}$.

With all of the above, we have

$$\begin{aligned} \bar{\mathbf{J}}(t) = -|e| \left\{ \Delta_p \left[\nabla_{\mathbf{k}} \epsilon_+(\mathbf{k})|_{\mathbf{K}-\mathbf{A}(t)} - \nabla_{\mathbf{k}} \epsilon_-(\mathbf{k})|_{\mathbf{K}-\mathbf{A}(t)} \right] \right. \\ \left. + |e| E(t) \left[-2 \Delta_p \Omega_-(\mathbf{K} - \mathbf{A}(t)) + \frac{2\pi \mathcal{C}_-}{V_{BZ}} \right] \hat{e}_x \right\}. \end{aligned} \quad (21)$$

The anomalous current only has component in the direction perpendicular to the laser field, while the intraband current essentially has component along the laser field (for zero second next neighbour hopping, the intraband current will be directed entirely along the laser field direction). In this way, we can neglect the component of the intraband current along the direction perpendicular to the laser field and conveniently separate the current as

$$\bar{\mathbf{J}}(t) \approx j_{\text{anom}}(t) \hat{e}_x + j_{\text{intra}}(t) \hat{e}_y, \quad (22)$$

with

$$\begin{aligned} j_{\text{anom}}(t) &= -|e|^2 E(t) \left[-2 \Delta_p \Omega_-(\mathbf{K} - \mathbf{A}(t)) + \frac{2\pi \mathcal{C}_-}{V_{BZ}} \right], \\ j_{\text{intra}}(t) &= -|e| \Delta_p \left[\nabla_{\mathbf{k}} \epsilon_+(\mathbf{k})|_{\mathbf{K}-\mathbf{A}(t)} - \nabla_{\mathbf{k}} \epsilon_-(\mathbf{k})|_{\mathbf{K}-\mathbf{A}(t)} \right]. \end{aligned} \quad (23)$$

The high harmonic spectrum will then be simply proportional to

$$\mathbf{D}(\omega) \propto \int e^{i\omega t} j_{\text{anom}}(t) dt \hat{e}_x + \int e^{i\omega t} j_{\text{intra}}(t) dt \hat{e}_y. \quad (24)$$

As explained in the main text, the intraband current does not play a role in the effect we want to explore. Therefore, we focus on the high harmonic spectrum obtained from the anomalous current:

$$j_{\text{anom}}(\omega) = -|e|^2 \int e^{-i\omega t} E(t) \left[-2\Delta_p \Omega_-(\mathbf{K} - \mathbf{A}(t)) + \frac{2\pi\mathcal{C}_-}{V_{BZ}} \right] dt. \quad (25)$$

We can expand the Berry connection in the Fourier components,

$$\Omega_-(\mathbf{k}) = \sum_{\mathbf{R} \in BL} e^{i\mathbf{k} \cdot \mathbf{R}} \Omega_-(\mathbf{R}), \quad (26)$$

where the sum runs over all integers of Bravais lattice vectors. Explicitly, we have

$$\begin{aligned} \Omega_-(\mathbf{K} - \mathbf{A}(t)) &= \sum_{\mathbf{R} \in BL} e^{i(\mathbf{K} + \mathbf{A}_0 \sin \omega_X t) \cdot \mathbf{R}} \Omega_-(\mathbf{R}) = \\ &= \sum_{\mathbf{R} \in BL} e^{i\mathbf{K} \cdot \mathbf{R}} \Omega_-(\mathbf{R}) \sum_{n=0}^{\infty} J_n(\mathbf{A}_0 \cdot \mathbf{R}) e^{in\omega_X t}, \end{aligned} \quad (27)$$

where J_n is the n -th Bessel function of the first kind and we have used the Jacobi-Anger expansion.

The anomalous current can now be expressed as

$$\begin{aligned} j_{\text{anom}}(\omega) &= -2\pi |e|^2 E_0 \left\{ \frac{2\pi\mathcal{C}_-}{V_{BZ}} [\delta(\omega - \omega_X) + \delta(\omega + \omega_X)] \right. \\ &\quad \left. - 2\Delta_p \sum_{n=0}^{\infty} \sum_{\mathbf{R} \in BL} e^{i\mathbf{K} \cdot \mathbf{R}} \Omega_-(\mathbf{R}) J_n(\mathbf{A}_0 \cdot \mathbf{R}) [\delta(\omega - (n+1)\omega_X) + \delta(\omega - (n-1)\omega_X)] \right\}. \end{aligned} \quad (28)$$

Finally, we arrive to the expressions of the harmonics emitted in the \hat{e}_x direction:

$$\begin{aligned} j_{\text{anom}}^{(1)}(\omega) &= -2\pi |e|^2 E_0 \left\{ \frac{2\pi\mathcal{C}_-}{V_{BZ}} - 2\Delta_p \sum_{\mathbf{R} \in BL} e^{i\mathbf{K} \cdot \mathbf{R}} \Omega_-(\mathbf{R}) [J_0(\mathbf{A}_0 \cdot \mathbf{R}) + J_2(\mathbf{A}_0 \cdot \mathbf{R})] \right\}, \\ j_{\text{anom}}^{(m>1)}(\omega) &= -2\pi |e|^2 E_0 \left\{ -2\Delta_p \sum_{\mathbf{R} \in BL} e^{i\mathbf{K} \cdot \mathbf{R}} \Omega_-(\mathbf{R}) [J_{m-1}(\mathbf{A}_0 \cdot \mathbf{R}) + J_{m+1}(\mathbf{A}_0 \cdot \mathbf{R})] \right\}. \end{aligned} \quad (29)$$

Acknowledgements R.E.F.S. and M.I. acknowledge support from EPSRC/DSTL MURI grant EP/N018680/1.

A.J.G and M.I. acknowledge support from the DFG QUTIF grant IV 152/6-1. O. Smirnova acknowledges

funding from DFG QUTIF grant SM 292/2-3. B.A. received funding from the European Union's Horizon 2020 research and innovation programme under grant agreement No. 706538.

1. Krausz, F. & Ivanov, M. Attosecond physics. *Reviews of Modern Physics* **81**, 163–234 (2009).
URL <https://link.aps.org/doi/10.1103/RevModPhys.81.163>.
2. Corkum, P. B. Plasma perspective on strong field multiphoton ionization. *Physical Review Letters* **71**, 1994–1997 (1993). URL <https://link.aps.org/doi/10.1103/PhysRevLett.71.1994>.
3. Lewenstein, M., Balcou, P., Ivanov, M. Y., L'Huillier, A. & Corkum, P. B. Theory of high-harmonic generation by low-frequency laser fields. *Physical Review A* **49**, 2117–2132 (1994).
URL <https://link.aps.org/doi/10.1103/PhysRevA.49.2117>.
4. Ghimire, S. *et al.* Observation of high-order harmonic generation in a bulk crystal. *Nature Physics* **7**, 138 EP – (2010). URL <http://dx.doi.org/10.1038/nphys1847>.
5. Popmintchev, T. *et al.* Bright coherent ultrahigh harmonics in the keV x-ray regime from mid-infrared femtosecond lasers. *Science* **336**, 1287–1291 (2012). URL <http://science.sciencemag.org/content/336/6086/1287>. <http://science.sciencemag.org/content/336/6086/1287.full.pdf>.
6. Ivanov, M. & Pisanty, E. Taking control of polarization. *Nature Photonics* **8**, 501 EP – (2014).
URL <http://dx.doi.org/10.1038/nphoton.2014.141>.

7. Jiménez-Galán, Á. *et al.* Control of attosecond light polarization in two-color bicircular fields. *Physical Review A* **97**, 023409– (2018). URL <https://link.aps.org/doi/10.1103/PhysRevA.97.023409>.
8. Hickstein, D. D. *et al.* Non-collinear generation of angularly isolated circularly polarized high harmonics. *Nature Photonics* **9**, 743 EP – (2015). URL <http://dx.doi.org/10.1038/nphoton.2015.181>.
9. Kfir, O. *et al.* Generation of bright phase-matched circularly-polarized extreme ultraviolet high harmonics. *Nature Photonics* **9**, 99 EP – (2014). URL <http://dx.doi.org/10.1038/nphoton.2014.293>.
10. Gariépy, G. *et al.* Creating high-harmonic beams with controlled orbital angular momentum. *Physical Review Letters* **113**, 153901– (2014). URL <https://link.aps.org/doi/10.1103/PhysRevLett.113.153901>.
11. Smirnova, O. *et al.* High harmonic interferometry of multi-electron dynamics in molecules. *Nature* **460**, 972 EP – (2009). URL <http://dx.doi.org/10.1038/nature08253>.
12. Baker, S. *et al.* Probing proton dynamics in molecules on an attosecond time scale. *Science* **312**, 424–427 (2006). URL <http://science.sciencemag.org/content/312/5772/424>. <http://science.sciencemag.org/content/312/5772/424.full.pdf>.
13. Shafir, D. *et al.* Resolving the time when an electron exits a tunnelling barrier. *Nature* **485**, 343 EP – (2012). URL <http://dx.doi.org/10.1038/nature11025>.

14. Pedatzur, O. *et al.* Attosecond tunnelling interferometry. *Nature Physics* **11**, 815 EP – (2015).
URL <http://dx.doi.org/10.1038/nphys3436>.
15. Mairesse, Y. *et al.* High harmonic spectroscopy of multichannel dynamics in strong-field ionization. *Physical Review Letters* **104**, 213601– (2010). URL <https://link.aps.org/doi/10.1103/PhysRevLett.104.213601>.
16. Haessler, S. *et al.* Attosecond imaging of molecular electronic wavepackets. *Nature Physics* **6**, 200 EP – (2010). URL <http://dx.doi.org/10.1038/nphys1511>.
17. Schubert, O. *et al.* Sub-cycle control of terahertz high-harmonic generation by dynamical bloch oscillations. *Nature Photonics* **8**, 119 EP – (2014). URL <http://dx.doi.org/10.1038/nphoton.2013.349>.
18. Luu, T. T. *et al.* Extreme ultraviolet high-harmonic spectroscopy of solids. *Nature* **521**, 498 EP – (2015). URL <http://dx.doi.org/10.1038/nature14456>.
19. Vampa, G. *et al.* All-optical reconstruction of crystal band structure. *Physical Review Letters* **115**, 193603– (2015). URL <https://link.aps.org/doi/10.1103/PhysRevLett.115.193603>.
20. Tancogne-Dejean, N., Mücke, O. D., Kärtner, F. X. & Rubio, A. Impact of the electronic band structure in high-harmonic generation spectra of solids. *Physical Review Letters* **118**, 087403– (2017). URL <https://link.aps.org/doi/10.1103/PhysRevLett.118.087403>.

21. McDonald, C. R., Vampa, G., Corkum, P. B. & Brabec, T. Interband bloch oscillation mechanism for high-harmonic generation in semiconductor crystals. *Physical Review A* **92**, 033845– (2015). URL <https://link.aps.org/doi/10.1103/PhysRevA.92.033845>.
22. Bauer, D. & Hansen, K. K. High-harmonic generation in solids with and without topological edge states. *Physical Review Letters* **120**, 177401– (2018). URL <https://link.aps.org/doi/10.1103/PhysRevLett.120.177401>.
23. Silva, R. E. F., Blinov, I. V., Rubtsov, A. N., Smirnova, O. & Ivanov, M. High-harmonic spectroscopy of ultrafast many-body dynamics in strongly correlated systems. *Nature Photonics* (2018). URL <https://doi.org/10.1038/s41566-018-0129-0>.
24. Liu, H. *et al.* High-harmonic generation from an atomically thin semiconductor. *Nature Physics* **13**, 262 EP – (2016). URL <http://dx.doi.org/10.1038/nphys3946>.
25. Luu, T. T. & Wörner, H. J. Measurement of the berry curvature of solids using high-harmonic spectroscopy. *Nature Communications* **9**, 916 (2018). URL <https://doi.org/10.1038/s41467-018-03397-4>.
26. Vampa, G. *et al.* Theoretical analysis of high-harmonic generation in solids. *Physical Review Letters* **113**, 073901– (2014). URL <https://link.aps.org/doi/10.1103/PhysRevLett.113.073901>.
27. Barth, I. & Smirnova, O. Nonadiabatic tunneling in circularly polarized laser fields: Physical picture and calculations. *Physical Review A* **84**, 063415– (2011). URL <https://link.aps.org/doi/10.1103/PhysRevA.84.063415>.

28. Barth, I. & Smirnova, O. Nonadiabatic tunneling in circularly polarized laser fields. ii. derivation of formulas. *Physical Review A* **87**, 013433– (2013). URL <https://link.aps.org/doi/10.1103/PhysRevA.87.013433>.
29. Cireasa, R. *et al.* Probing molecular chirality on a sub-femtosecond timescale. *Nature Physics* **11**, 654 EP – (2015). URL <http://dx.doi.org/10.1038/nphys3369>.
30. Hartung, A. *et al.* Electron spin polarization in strong-field ionization of xenon atoms. *Nature Photonics* **10**, 526 EP – (2016). URL <http://dx.doi.org/10.1038/nphoton.2016.109>.
31. Xie, X. *et al.* Internal momentum state mapping using high harmonic radiation. *Physical Review Letters* **101**, 033901– (2008). URL <https://link.aps.org/doi/10.1103/PhysRevLett.101.033901>.
32. Eckart, S. *et al.* Ultrafast preparation and detection of ring currents in single atoms. *Nature Physics* (2018). URL <https://doi.org/10.1038/s41567-018-0080-5>.
33. Nagaosa, N., Sinova, J., Onoda, S., MacDonald, A. H. & Ong, N. P. Anomalous hall effect. *Reviews of Modern Physics* **82**, 1539–1592 (2010). URL <https://link.aps.org/doi/10.1103/RevModPhys.82.1539>.
34. Hasan, M. Z. & Kane, C. L. Colloquium. *Reviews of Modern Physics* **82**, 3045–3067 (2010). URL <https://link.aps.org/doi/10.1103/RevModPhys.82.3045>.

35. Haldane, F. D. M. Model for a quantum hall effect without landau levels: Condensed-matter realization of the "parity anomaly". *Physical Review Letters* **61**, 2015–2018 (1988). URL <https://link.aps.org/doi/10.1103/PhysRevLett.61.2015>.
36. Kane, C. L. & Mele, E. J. \mathbb{Z}_2 topological order and the quantum spin hall effect. *Physical Review Letters* **95**, 146802– (2005). URL <https://link.aps.org/doi/10.1103/PhysRevLett.95.146802>.
37. Mak, K. F., McGill, K. L., Park, J. & McEuen, P. L. The valley hall effect in mos2 transistors. *Science* **344**, 1489–1492 (2014). URL <http://science.sciencemag.org/content/344/6191/1489>. <http://science.sciencemag.org/content/344/6191/1489.full.pdf>.
38. Jotzu, G. *et al.* Experimental realization of the topological haldane model with ultracold fermions. *Nature* **515**, 237 EP – (2014). URL <http://dx.doi.org/10.1038/nature13915>.
39. Sala, S., Förster, J. & Saenz, A. Ultracold-atom quantum simulator for attosecond science. *Physical Review A* **95**, 011403– (2017). URL <https://link.aps.org/doi/10.1103/PhysRevA.95.011403>.
40. Garg, M. *et al.* Multi-petahertz electronic metrology. *Nature* **538**, 359 EP – (2016). URL <http://dx.doi.org/10.1038/nature19821>.

41. Castro Neto, A. H., Guinea, F., Peres, N. M. R., Novoselov, K. S. & Geim, A. K. The electronic properties of graphene. *Reviews of Modern Physics* **81**, 109–162 (2009). URL <https://link.aps.org/doi/10.1103/RevModPhys.81.109>.
42. Xiao, D., Chang, M.-C. & Niu, Q. Berry phase effects on electronic properties. *Rev. Mod. Phys.* **82**, 1959–2007 (2010). URL <https://link.aps.org/doi/10.1103/RevModPhys.82.1959>.
43. Ashcroft, N. & Mermin, N. *Solid State Physics* (Cengage Learning, 2011).